I R A M P
6(1), June 2015, pp. 43-55

ISSN: 2229-3159

Radial electron density measurements in laser-induced plasma from Abel inverted hydrogen Balmer beta line profiles

CHRISTIAN G. PARIGGER, GHANESHWAR GAUTAM AND DAVID M. SURMICK

Center for Laser Applications University of Tennessee Space Institute
411 B.H. Goethert Parkway Tullahoma, TN 37388

ABSTRACT: Time-resolved emission spectroscopy is applied to obtain radial electron density values in laser-induced plasma. Hydrogen beta line profiles are recorded following optical breakdown in ultra-high-pure hydrogen gas. Asymmetric Abel inversion techniques are utilized in the analysis of data collected for the time delay of 400 ns for the purpose of investigating the spatial plasma distribution. The averaged, line-of-sight electron densities are found to be in the range of 1 to 2.5 × 10^{17}cm^{-3}. The electron density distributions reveal spherical shell structures and indicate a factor of 2 variation across the close to spherically symmetric expanding laser-induced plasma.

PACS Codes: 32.70.Jz, 33.70.Jg, 78.47.D-, 51.50.+v

KEYWORDS: Line shapes and widths, laser-induced breakdown spectroscopy, laser-induced plasma, time-resolved spectroscopy, Abel inversion, hydrogen Balmer series, electron density

1. INTRODUCTION

In various applications of laser-induced plasma, measurements of emission spectra are designed to determine sample composition [1]. Evaluations of plasma characteristics such as electron temperature, T_e, or electron density, N_e, frequently rely on line-of-sight diagnostics. Noteworthy is also the interest in generating astrophysical conditions in the laboratory for the study of, for example, white dwarf [2,3] photospheric conditions at $T_e \sim 1$ eV, utilizing hydrogen beta line profiles for measurement of $N_e \sim 1 \times 10^{17}$cm^{-3}. For well-established plasma sources and in the study of laser-induced plasma, inversion algorithms can be implemented to fully describe the thermodynamic state and/or species distribution. General approaches make use of the so-called Radon transform and Radon inversion [4-9], especially for situations that require projections along several directions to assemble a comprehensive map of the source. Some of the Radon inverse transform implementations [7-9] are dedicated to medical diagnosis, or are in use for the characterization of nuclear radiation sources, and have been applied successfully in the characterization of laser-induced plasma [10].

In this work, radiation from a Nd: YAG Q-switched device is focused with a single lens to an irradiance of sufficient magnitude for optical breakdown to occur. The spatial distribution of the electron density is of interest in conjunction with possible simplifications of the inverse algorithm due to symmetries of the experimental arrangement. In an idealized focusing arrangement that describes a clean laser beam and a reasonable low ratio of beam diameter and of focal length, the usual presumptions include a symmetric peak-irradiance distribution together with a diffraction-limited, point-like initiation of plasma. For that reason, the one-parameter Radon transform, or Abel transform, is considered. Strictly following the definition of the Abel transform, lateral symmetry is required for the inversion of the line-of-sight integrated signals. Both self-absorption and Abel inversion have been previously discussed in the context of laser-induced breakdown spectroscopy [11]. However, slight asymmetries are acceptable along the line of sight integration. New algorithms [12, 13] and symmetric and asymmetric Abel inversions [14, 15] can be adapted and utilized in the analysis of the Balmer series hydrogen beta data that were recorded using time-resolved laser spectroscopy.

In the set of experiments performed in this work, time-resolved line-profiles of the Balmer series hydrogen beta transition, H_β, are recorded for the purpose of determining the variation of the electron density along the line of sight. The laser-induced plasma is generated by guiding the laser beam parallel to the spectrometer slit. For sufficient irradiance, a plasma is generated that extends along the slit. With 1.05:1 plasma imaging and a slit width of 50 μm, a slice of 52.5 μm width of the plasma is dispersed by a holographic grating and recorded with an intensified, two-dimensional array detector comprised of 1024 × 1024 pixels. The horizontal dimension of this detector is used to record the spectra, and the vertical dimension is used to spatially resolve the plasma emissions along the slit height. This geometry is selected for investigations of the line-of-sight contributions from the center slice with Abel inverse transforms. The spatially resolved spectra along the slit height are utilized to find, first, the radial distribution of the spectra within the imaged slice by applying the Abel inversion of the data for each dispersed wavelength, and second, the electron density distribution from fitting the spatially resolved spectra to known hydrogen beta profiles [16-18].

Shadowgraph and Schlieren measurements of laser-induced plasma in standard ambient temperature and pressure laboratory air show close to spherically symmetric plasma cores for time delays of 100 to 10,000 ns [19, 20]. The plasma cores reveal internal structure over and above plasma dynamic separation of the shock wave [19, 20]. The laser-induced hydrogen plasma for a time delay of 400 ns also deviates from perfect spherical symmetry. In this work, the contributions along the line-of-sight for the narrow center slice are modeled to be circularly symmetric while allowing slight deviation from this symmetry.

The Abel transform in three dimensions describes the integral transform associated with line-of-sight experiments for spherically symmetric plasma, however, using the projection onto the xz-plane reduces the Abel transform from three to two dimensions. Suppose a lateral distribution of a physical state can only be measured by means of an average and/or line-of-sight [13] with an integral equation

$$I(z) = 2\int_z^R f(r)\frac{r}{\sqrt{r^2 - z^2}}dr, \tag{1}$$

where *I(z)* and *f(r)* denote the measured lateral (along the slit height, *z*) and radial intensity distributions, respectively. The upper integration limit, *R*, is usually much larger than the circularly symmetric projection dimension, δ, or in other

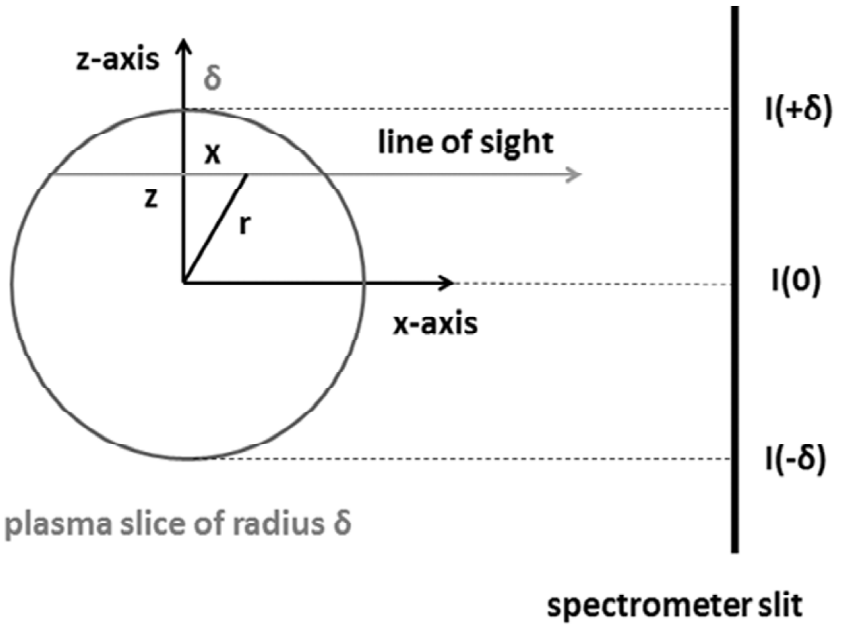

Figure 1: Geometry for reconstruction of the line-of-sight measurements with Abel inverse transforms of Equation (1)

words $R \gg \delta$. The factor of 2 indicates top/bottom symmetry. Figure 1 elucidates the geometry details for the reconstruction of the recorded time-resolved emission data. The vertically recorded data of the ICCD images correspond to the slit height positions, and the horizontally recorded data correspond to the wavelengths of the spectra.

Equation (1) can be inverted using an analytical approach with derivatives, known as the Abel inverse transform. Differentiation however is usually difficult to accomplish for spectra. For that reason, a development into a complete set of orthogonal polynomials is designed jointly with a minimization procedure to find the development coefficients. Advantages of this method include [13] computation of the Abel inverse transform without the need for differentiation and without the need for pre-treating the recorded data, leading to inverted intensity values, *I(r)*, with errors of only a few percent for selected test cases [13]. The requirement for circular symmetry can be softened in that top and bottom sections can show differences [15]. One would define a symmetric contribution and also correct for the top to bottom asymmetry. This is accomplished by introducing a symmetrized profile, $I_0(z)$, following the identical analysis procedure discussed by Blades [15],

$$I_0(z) = [I(z) + I(-z)]/2, \tag{2}$$

with the corresponding asymmetric portions

$$G(\pm z) = I(\pm z)/I_0(z). \tag{3}$$

Subsequent to finding the Abel inverse transform of $I_0(z)$ to find $I_0(r)$, the asymmetric profiles can be computed from

$$I(r, \pm z) = G(\pm z) I_0(r). \tag{4}$$

This approach has been applied especially for extracting subtle differences that are of interest in rigorous analysis. Of course, comparisons of the symmetrized profile and asymmetric Abel inverse tranformed results are required to justify this approach. For the 400 ns time delay, the asymmetry turns out to be minimal for the center region of the plasma.

With a two-dimensional array detector coupled to a Czerny-Turner type spectrometer, lateral data can be recorded without the need of moving the spectrometer. The plasma core deviates slightly from spherical symmetry for the investigated time delays, and therefore, measurements at different angles or for different slices would be required for complete and exact reconstruction of the three-dimensional plasma distribution at a specific time delay. In this work, results are presented for reconstruction from line-of-sight measurements for the near circularly symmetric center slice for the zx-plane projection of the three dimensional plasma. The slice thickness corresponds to the slit width for close to 1:1 imaging.

For the computation of the Abel inverse transform, one can employ the projection-slice theorem that can be discussed with the Fourier-Hankel-Abel-transform cycle, or one can rely on a complete series of functions [13] mentioned above. For the analysis of the accumulated spectra and without further application of digital filters, selected Chebyshev series composed of first kind Chebyshev polynomials yield the variation of the emissivity with wavelength, subsequently the electron density can be determined from the laterally resolved hydrogen beta lines. The specific orthogonal, complete series minimizes the error excursions [21], as anticipated from the use of Chebyshev polynomials. The applied method is based on the development of the Abel inverse transform in terms of a series that includes pre-calculated transforms. In the process of least square fitting the recorded data to these transforms, one specifies the number of terms to be included in the series. The number of terms that are included in the series solution affects the accuracy and noise. The more terms that are considered the higher the noise for the wavelength-dependent emissivity. Most importantly, the particular series solution approach that shows discrepancies in the recovered function of the order of a few percent, has been formalized in a Matlab® script [12] that alleviates the implementation of the Abel inverse transform.

2. EXPERIMENTAL DETAILS

For the experimental studies, laser-induced optical breakdown was initiated in ultra-high-pure (UHP) hydrogen gas of 99.999 % purity contained in a cell at a pressure of 1.08×10^5 Pa (810 Torr). This particular hydrogen pressure

was selected as well in a previously communicated detailed study of hydrogen beta line profiles following laser-induced breakdown [22]. Prior to filling the cell with hydrogen, evacuation to pressures of the order of 10^{-4} Pa (10^{-6} Torr) was accomplished to obtain a vacuum that is typically in use for preparing cells for discharges. A Q-switched Nd: YAG laser (DCR-2A(10) PS; Quanta-Ray) was operated at the fundamental wavelength of 1064 nm and was focused with an f-number of 10 (f/10) using a 125 mm focal length lens through the Quartz windows, with the laser beam entering the cell from the top or parallel to the slit.

For the imaging of the plasma, a single lens was positioned for 1.05:1 imaging with an effective focusing speed of 5.6 to match the f-number of the 0.64 m Jobin-Yvon, Czerny-Turner spectrometer. A 1200 groves/mm holographic grating was used in conjunction with an intensified Charge-Coupled-Device (iCCD, Andor iStar) that resulted in a spectral resolution of 0.1 nm. The iCCD shows a pixel resolution of 1024 × 1024, with the horizontal 1024 pixels corresponding to the wavelength. With 8-pixel binning, the vertical 128 regions correspond to the location in the plasma column. The camera software was utilized to record signals from 50 consecutive events, to background correct the spectra, and to invert the vertical dimension such that top of the image is identical with the top of the plasma (toward the focusing lens of the Nd: YAG beam). The wavelength and relative intensity calibrations were accomplished with standard light sources and with a calibrated deuterium/ tungsten lamp.

The region of interest spanned 5.5 mm for the plasma initiated with 120 mJ, 13 ns pulses, and for a time delay of 400 ns. This particular time delay from optical breakdown results in practically identical results for line-of-sight averaged electron densities [22] when using the Griem and the Oks theories. Moreover, the Balmer series hydrogen beta line can be nicely captured by the spectrometer/detector arrangement. In terms of the 8-pixel binning, 50 spectra of 0.11 mm height were recorded in this study of the hydrogen beta line profiles. The arrangement is similar to a recently reported experimental investigation of laser-induced plasma in air [23].

Due to residual moisture in standard ambient temperature and pressure laboratory air, the hydrogen beta line can be relatively easily detected but for time delays of the order of 10 × longer from optical breakdown. Presence of oxygen and nitrogen in the laboratory air causes significantly more free electrons during the optical breakdown process, consequently, the hydrogen beta emissions can be easily demarcated for time delays of typically 5 μs. In air, nitrogen lines on the red side of the H_β line can affect the appearance of the free-electron background. In turn, use of UHP hydrogen allows one to study Balmer series hydrogen line profiles in detail.

It was also established previously, that self-absorption of the hydrogen beta line is insignificant [23] for electron densities of the order of 1×10^{17} cm^{-3}. The self-absorption assessment included the use of an additional lens and a mirror at the opposite side of the spectrometer, and by retro-reflection through the plasma, the effect of self-absorption could be quantified. Of course, self-absorption would not only cause a reduction of the measured peak-heights, but it would also modify and/or distort the line shapes. The differences of the full-width-half-maximum (FWHM) and of the hydrogen peak separations are well within the estimated error bars associated with electron density determination from the H_β line. These error bars amount to typically 5 to 10% for electron densities on the order of 0.5 to 3×10^{17} cm^{-3}. For comparison, self-absorption effects of the hydrogen alpha line [24, 25] would come into play for electron densities, N_e, of the order 20×10^{17} cm^{-3}-for such N_e values, the Balmer series hydrogen beta line can not be seen in emission. In recent work on symmetric hydrogen Balmer series lines [27] and especially for hydrogen beta [28], both FWHM and peak-separation can serve as means to determine the electron density.

3. RESULTS

The determination of the electron densities from the background-, wavelength-, and detector-sensitivity-calibrated data is categorized into two distinct approaches:

(i) Find N_e directly from the recorded line-of-sight set of data that are resolved vertically; and

(ii) Apply the Abel inverse transform first to obtain the radial, spectrally resolved emission spectra, and then infer the radial N_e variation.

3.1. Spatially resolved line-of-sight spectra

Figure 2 illustrates the recorded hydrogen beta line profiles for the time delay of 400 ns from the generation of optical breakdown in UHP hydrogen gas. The figure also indicates the fitted, asymmetric hydrogen lines together with the inferred electron densities at a slit height of 1.96 mm. The overall fits to the recorded spectra include the background contributions that are determined simultaneously with the best-fit, least-square hydrogen beta profiles.

The values for the electron density, FWHM, peak-separation, and ratio of FWHM are systematically determined by engaging a full-profile fit of the least-square kind, including allowance and fitting for a constant background. This constant background shows a very slight increase toward the blue side of the recorded wavelength range.

Figure 3 illustrates the inferred electron density *vs.* slit height. Table 1 lists the obtained results for N_e.

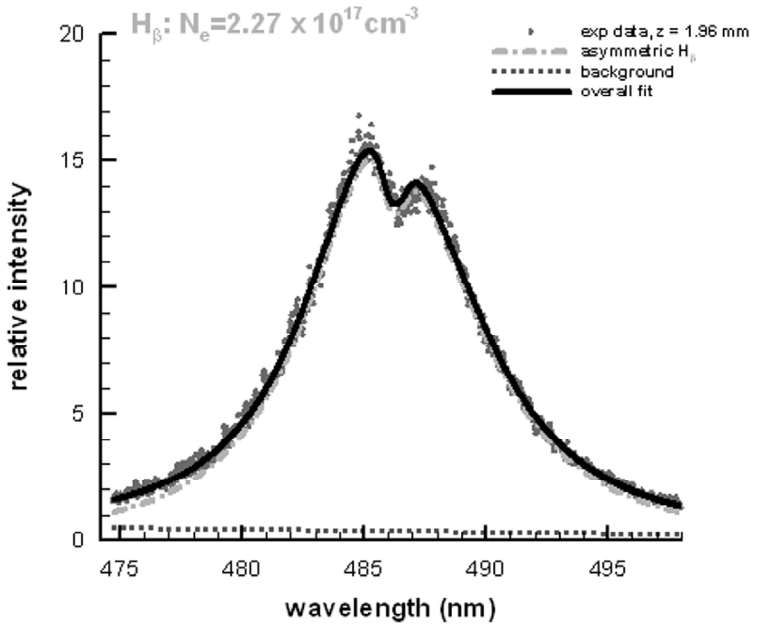

Figure 2: Line-of-sight measured and fitted hydrogen beta lines for a time delay of τ = 400 ns

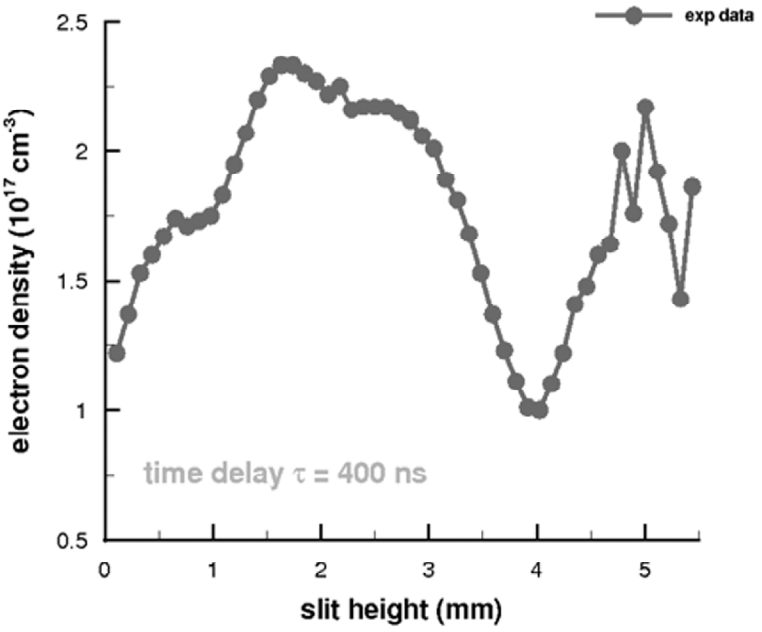

Figure 3: Electron densities *versus* slit height, *z*, inferred from full profile fitting of the line-of-sight measured H_β line for a time delay of τ = 400 ns.

Table 1
Slit height, z, H_β electron density, and full-width at half-maximum (FWHM) from full profile fitting. Included are results from the electron density, N_e^{FWHM}, obtained from Equation (6), and the ratio $r_{Ne} = N_e / N_e^{FWHM}$

z (mm)	N_e (10^{17}cm^{-3})	FWHM (nm)	N_e^{FWHM} (10^{17}cm^{-3})	r_{Ne}
0.11	1.22	5.10	1.19	1.02
0.22	1.37	5.47	1.32	1.04
0.33	1.53	5.93	1.48	1.04
0.44	1.60	6.16	1.56	1.03
0.54	1.67	6.39	1.64	1.02
0.65	1.74	6.63	1.73	1.01
0.76	1.71	6.53	1.69	1.01
0.87	1.73	6.60	1.71	1.01
0.98	1.75	6.67	1.74	1.01
1.09	1.83	6.95	1.84	0.99
1.20	1.95	7.37	2.00	0.97
1.31	2.07	7.79	2.17	0.96
1.41	2.20	8.26	2.35	0.94
1.52	2.29	8.58	2.48	0.92
1.63	2.33	8.72	2.54	0.92
1.74	2.33	8.72	2.54	0.92
1.85	2.30	8.62	2.50	0.92
1.96	2.27	8.51	2.45	0.93
2.07	2.22	8.33	2.38	0.93
2.18	2.25	8.44	2.42	0.93
2.28	2.16	8.11	2.29	0.94
2.39	2.17	8.15	2.31	0.94
2.50	2.17	8.15	2.31	0.94
2.61	2.17	8.15	2.31	0.94
2.72	2.15	8.08	2.28	0.94
2.83	2.12	7.97	2.24	0.95
2.94	2.06	7.76	2.15	0.96
3.05	2.01	7.58	2.08	0.96
3.16	1.89	7.16	1.92	0.98
3.26	1.81	6.88	1.82	1.00
3.37	1.68	6.43	1.65	1.02
3.48	1.53	5.93	1.48	1.04
3.59	1.37	5.47	1.32	1.04
3.70	1.23	5.12	1.20	1.03
3.81	1.11	4.86	1.12	1.00
3.92	1.01	4.67	1.05	0.96
4.03	1.00	4.66	1.05	0.95
4.13	1.10	4.84	1.11	0.99
4.24	1.22	5.10	1.19	1.02
4.35	1.41	5.58	1.35	1.04
4.46	1.48	5.78	1.42	1.04
4.57	1.60	6.16	1.56	1.03
4.68	1.64	6.29	1.60	1.02
4.79	2.00	7.55	2.07	0.97
4.90	1.76	6.70	1.75	1.00
5.00	2.17	8.15	2.31	0.94
5.11	1.92	7.26	1.96	0.98
5.22	1.72	6.56	1.70	1.01
5.33	1.43	5.64	1.37	1.04
5.44	1.86	7.05	1.88	0.99

The electron densities in Figure 3 are indicated with reference to the slit height that is measured from bottom to top. The propagation direction of the laser beam that induces optical breakdown is from top to bottom, or in the figure from right to left. The initial peak is associated with the emanating shockwave, followed by a region of diminished N_e and then a slightly increasing but relatively constant electron density prior to decreasing values of N_e for the laser plasma in the forward direction. The electron densities displayed in Fig. 3 are obtained from the line-of-sight data. The values of the electron densities were deduced from full-profile fitting using communicated line profiles [16]. The listed FWHM is determined from the fitted, asymmetric profiles by taking the mean of the two hydrogen beta peaks I_{red} and I_{blue},

$$I_{mean} = (I_{red} + I_{blue})/2, \tag{5}$$

and then finding the FWHM from ½ I_{mean}.

A recently published formula for the determination of the electron density from the FWHM is applied to provide an alternate value for N_e that includes estimated temperature values, with N_e (cm^{-3}), and the FWHM, Δλ(nm),

$$\Delta\lambda(H_\beta) = 4.50 \left(\frac{N_e}{10^{17}}\right)^{0.71 \pm 0.03}. \tag{6}$$

This formula was derived from tabulated values for the electron densities [22, 26]. The electron density results that were computed using Equation (6), N_e^{FWHM}, are also indicated in the table. One can see that the electron densities obtained from Eq. (6) agree with the full-profile fits from theory profiles in the temperature range of 10,000 K to 20,000 K within 8 %, or in practical terms within the accuracy of extracting the FWHM from moderately noisy hydrogen beta data. The average of the electron density inferred from the FWHM amounts to 1.83×10^{17}cm^{-3} which is in within 5% of the results from a previous study of line-of-sight averaged spectra for the selected pressure and time delay [22].

Figure 4 illustrates the recorded image data corresponding to the results in Table (1) using pseudo-colored contours for the slit height magnitudes of 0.11 mm to 5.44 mm and for the spectral range of 474.4 nm to 497.8 nm.

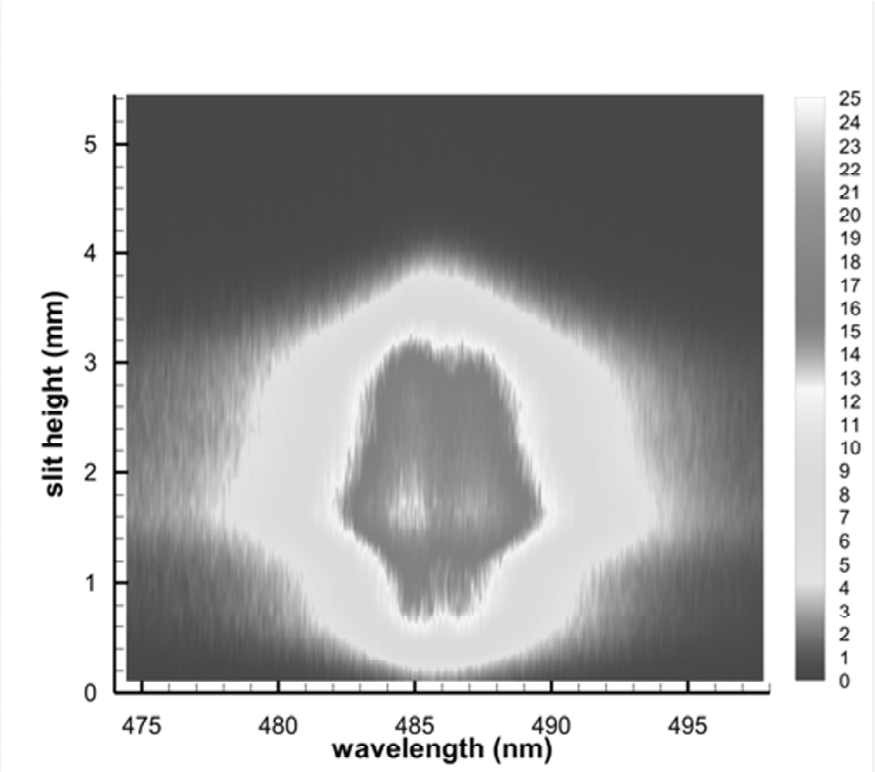

Figure4: Contour image of the recorded hydrogen beta line for a time delay of τ = 400 ns

The inferred electron densities for the 4.0 mm to 5.4 mm region are included in the table, yet due to the signal-to-noise ratio in this region, the N_e values show slightly larger error margins than for the 0.11 mm to 4.0 mm region. The color palette on the right side indicates the range of intensities. The double-peak spectra of the hydrogen beta line are clearly discernible at slit heights near 1.5 mm.

The best-fit profiles of the line-of-sight data clearly indicate visually excellent results for the time delay of 400 ns, and equally, would show excellent results for time delays of 650 ns. The Abel inverse transforms of the 400 ns data show less noise than the 650 ns data, in part due to the typically a factor of 1.5 wider spectral profiles for the recorded data at a time delay of 400 ns. Therefore, the Abel inverse transform of the data for a delay time of 400 ns are further elaborated in detail. For a time delay of 150 ns, the electron density is determined from partial hydrogen beta profiles. An electron density of 7.5×10^{17} cm^{-3} corresponds to a FWHM of 18.8 nm as calculated using Equation (6), therefore, a wavelength range of 1.28 × this width is covered by the 24 nm spectral window of the spectrometer-detector system for the experiments reported here.

3.2. Abel inverted spectra

The radial electron density variation is of interest, for instance, in the evaluation of whether an equilibrium distribution is indeed reasonable. The determination of electron density of course supposes optically thin scenarios. In previous communications, the hydrogen beta line profile was discussed to be optically thin for time delays of the order of 5 μs in air breakdown and for densities of the order of 1×10^{17} cm^{-3}. The 400 ns time delay hydrogen beta data recorded from optical breakdown in ultra-high-pure hydrogen gas, the corresponding time delays are of the order of 1/10 of the time delays used for air breakdown. However, self-absorption is not considered to be of significance when evaluating the error bars associated with electron density determination. A method for evaluating whether self-absorption occurs has been recently communicated by means of comparing the electron densities obtained from the peak separation with the ones obtained from the FWHM. In Table 1, a detailed list of FWHM values is included, yet it is emphasized that the H_β profiles were fit using full profiles, subsequently, the widths were extracted from these fitted profiles.

The Abel inversion is accomplished by utilizing a polynomial expansion combined with a recently made available script [12, 13] for the software package Matlab®. The spectra that were recorded vertically were utilized for the Abel inversion. For each wavelength, values along the slit-axis are utilized to derive the radial profile, or, the wavelength emissivity is resolved radially. In the application of the Abel inversion, slight asymmetries [15] for the bottom and top half are included as well. Advantages of using this particular implementation include that special filtering of the recorded data is not required. However, it is noted that a reasonable signal to noise ratio of the data set would be required for obtaining visual agreement with the typical asymmetric appearance of hydrogen beta line profiles in laser-induced optical breakdown spectroscopy for electron densities larger than 0.1 to 0.5×10^{17} cm^{-3}. Of course, the double peak structure is of fundamental nature as well, and in principle, is a function of the resolution of the instrument. For Stark-broadened line profiles in applied LIBS studies, electron densities from double peaked hydrogen beta lines are typically determined for electron densities in the range of 0.5 to 5×10^{17} cm^{-3}. For electron densities in the range of 0.1 to 100×10^{17} cm^{-3}, the hydrogen alpha line is frequently used as well, although care needs to be exercised for values higher than 20×10^{17} cm^{-3} due to H_α self-absorption [24, 25].

Figure 5 illustrates the results from applying the Abel inversion algorithm. The symmetric electron density profile is obtained from the symmetrized measured lateral data $I_0(z)$ (see Eq. (2)). The asymmetric profile is reconstructed with the asymmetry portions $G(\pm z)$ (see Eqs. (3) and (4)) and a close to symmetric profile is obtained. In Fig. 5, negative values for r are used to conveniently display the differences of symmetric and of asymmetric results. The radial position $r = 0$ denotes the center of the plasma slice and it corresponds to the lateral slit height $z = 2.18$ mm. Abel inversions are computed for the lateral slit range $z_{low} = 0.22$ mm to $z_{high} = 4.14$ mm, corresponding to the circularly symmetric plasma slice of radius $\delta = 1.96$ mm for the 400 ns time delay data (see Fig. 4).

At the center, there is a peak in electron density, flanked by maxima, and including a clear peak near $r = 1.6$ mm. The maxima near the $r = \pm 0.54$ mm positions are associated with the breakdown kernel or the very center

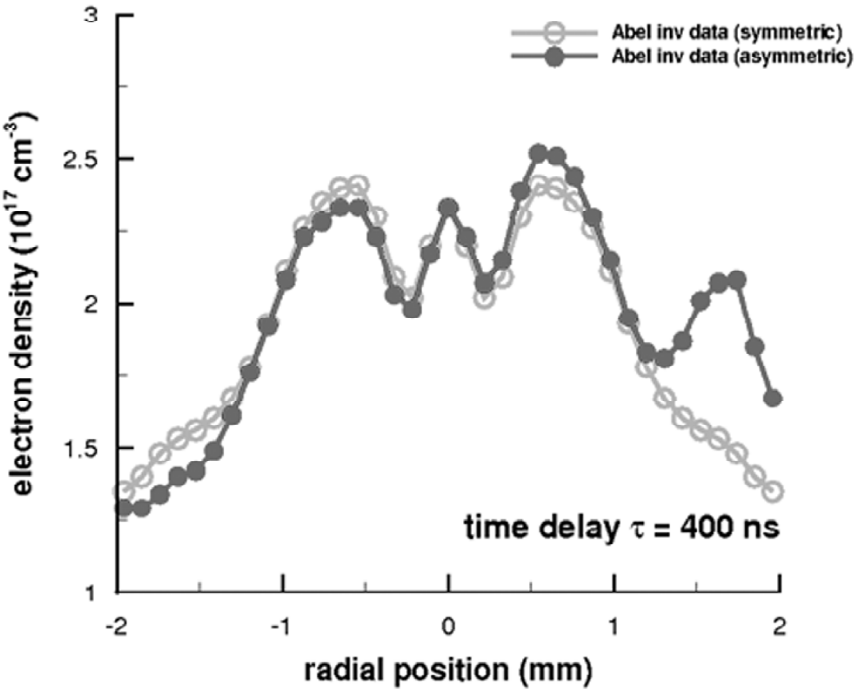

Figure 5: Electron densities versus radial position, inferred from Abel inversion of the recorded H_β line profiles for a time delay of τ = 400 ns

(viz. epicenter) of the generation of laser-induced breakdown. In view of the spherical symmetry, the peaks at $r = \pm$ 0.54 mm indicate a ring structure for electron density in the plasma. The extra peak near r = 1.6 mm denotes an increased electron density, possibly due to expanding shockwave phenomena and/or due to the specific focusing characteristics of the Nd: YAG beam shape that was used. There is an ever so slight decrease in asymmetric electron density near r =-1.6 mm adjacent to the obvious increase near the r = + 1.6 mm position. The beam profile resembles a so-called doughnut mode as a result of the specific optical arrangement of the Quanta Ray Nd: YAG laser device that further shows a beam profile with a preferred intensity distribution on one side, in part leading to the asymmetry in the electron density. Other reasons for the occurrence of an asymmetry can be the variations of optical breakdown processes during the capture of an average of 50 consecutive laser-induced plasma events during the experiments. For close to perfect Nd:YAG laser beams, such as the ones used for high-power Particle-Imaging-Velocimetry systems, where close to Gaussian TEM_{00} mode structures are available in conjunction with low M^2 values, the peaks near the positions $r = \pm$ 1.6 mm would be expected to be similar to the results portrayed in Figure 5. In future experiments that utilize close to TEM_{00} Nd: YAG laser radiation, the measured electron density profiles would be expected to be close to symmetric with respect to the center position. For the reconstruction of the three-dimensional plasma distribution, measurement of more lateral slices or measurements at different angles would be needed to further explore and accurately determine the slight electron density asymmetry near the center that is caused by the radiative energy deposition for the generation of laser-induced plasma. The asymmetric energy deposition leads to fluid dynamics phenomena including the development of vortices that have been measured for 10's to 100's of microseconds after air breakdown.

The Abel inverse transforms for spectral emissions are further discussed. Usually, data needs to be digitally filtered in a reasonable manner prior to engaging Abel inversion algorithms. However, such filtering is not applied, yet an average of 50 consecutive laser-plasma events were collected to improve the signal-to-noise ratio. For example, the 400 ns time delay spectra for the radial positions of r = -0.54 mm and r = + 0.54 mm are easily recognizable as Balmer series hydrogen beta lines. Figures 6 and 7 illustrate the Abel inverted emission and fitted hydrogen beta line profiles.

The electron density is ~ 10% lower for r = –0.54 mm than for r = + 0.54 mm, indicating a circular asymmetry of ~ 10%. Near the edges of the plasma, smaller signals will cause more noise for the Abel inverse transform.

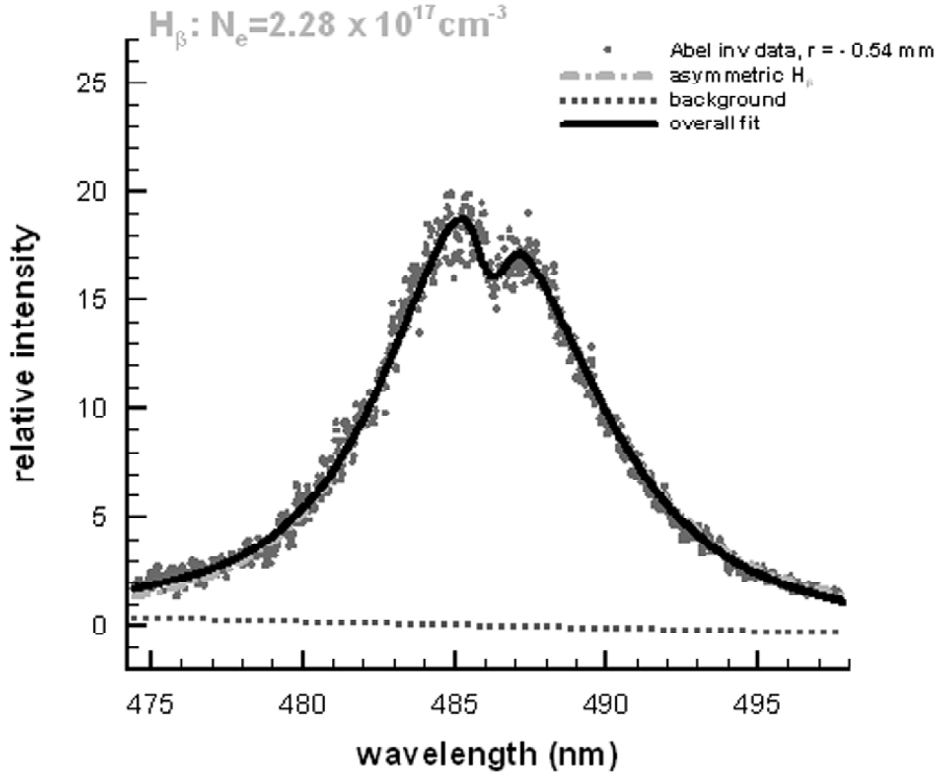

Figure 6: The electron density of 2.28 × 10^{17} cm^{-3} at the position r = -0.54 mm is inferred from the Abel inverted data for the time delay of τ = 400 ns

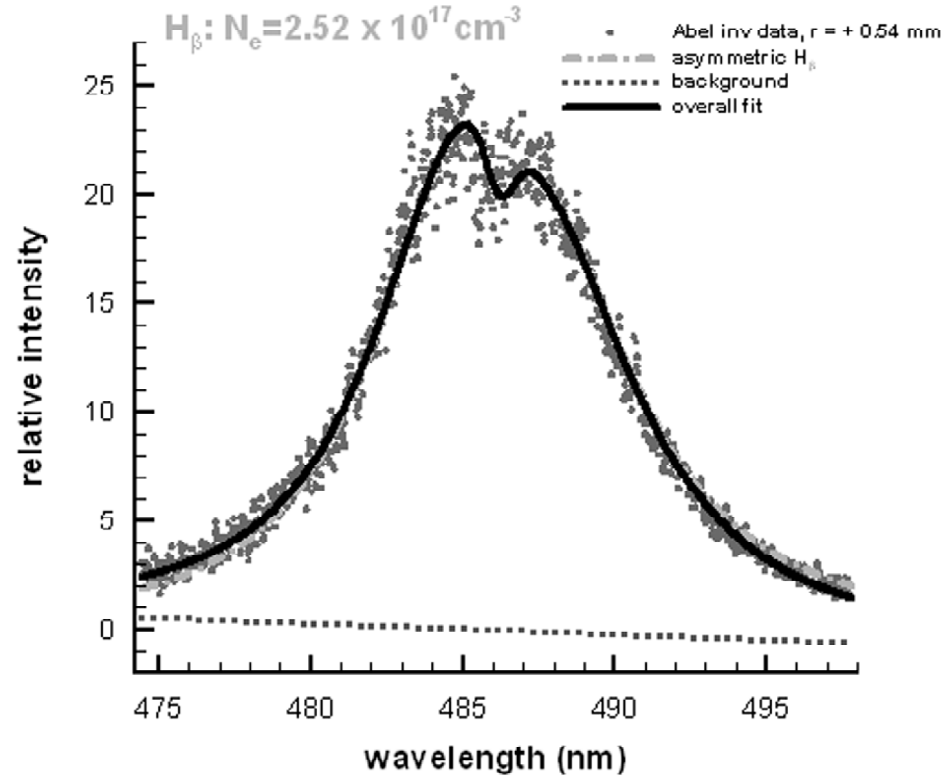

Figure 7: The electron density of 2.52 × 10^{17} cm^{-3} at the position r = + 0.54 mm is inferred from the Abel inverted data for the time delay of τ = 400 ns

Equally, choice of extra terms in the Chebyshev series would increase the precision, but would also increase unnecessary details or noise that would pose difficulties in the determination of the electron density values. For that reason, the number of terms, N, selected for this Abel inversion analysis amounted to $N = 10$.

The Abel inversion is also applied for the time delays of 150 ns and 650 ns. Figure 8 illustrates the results. For the early 150 ns time delay data, the profiles are nearly symmetric in the center region, except for higher electron density values near $r = +1.62$ mm that are likely due to the specific beam shape of the Nd: YAG radiation. However, there is also a slight peak near $r = -1.62$ mm which would further indicate phenomena associated with the plasma expansion following laser-induced breakdown.

The center portion reveals a diminished electron density with peaks on either side of center, which would indicate near circular symmetric electron densities of the imaged plasma slice, implying near spherical symmetry inside the volume bounded by the expanding shock that can be recorded with shadowgraph-or Schlieren-imaging. In view of Fig. 5, the electron density near line center reduces with increasing time delay while sustaining maxima near the $r = \pm 0.54$ mm positions. This is also seen in the expanded electron density values (use right vertical axis) obtained from the 650 ns data although there are only slight indications of local maxima. One may infer from the indicated results for the electron densities that a standing electron wave pattern is created. Averages from 50 consecutive laser breakdown events and slight variations from event to event can easily wash out this pattern for longer time delays.

Furthermore, for the higher electron density of nearly 10×10^{17}cm^{-3} ($N_e$axis on the left) increased errors occur in the N_e determination. The distribution of the electron density at line center reveals smaller electron density near $r = 0$ mm early in the plasma decay, with higher electron density away from center. While the determination of the electron density near center shows reasonable errors (see Eq. (6)) and due to a value for $N_e$of the order of 5×10^{17}cm^{-3}, a diminished electron density at $r = 0$ mm position is inferred. In future experiments, the variation of

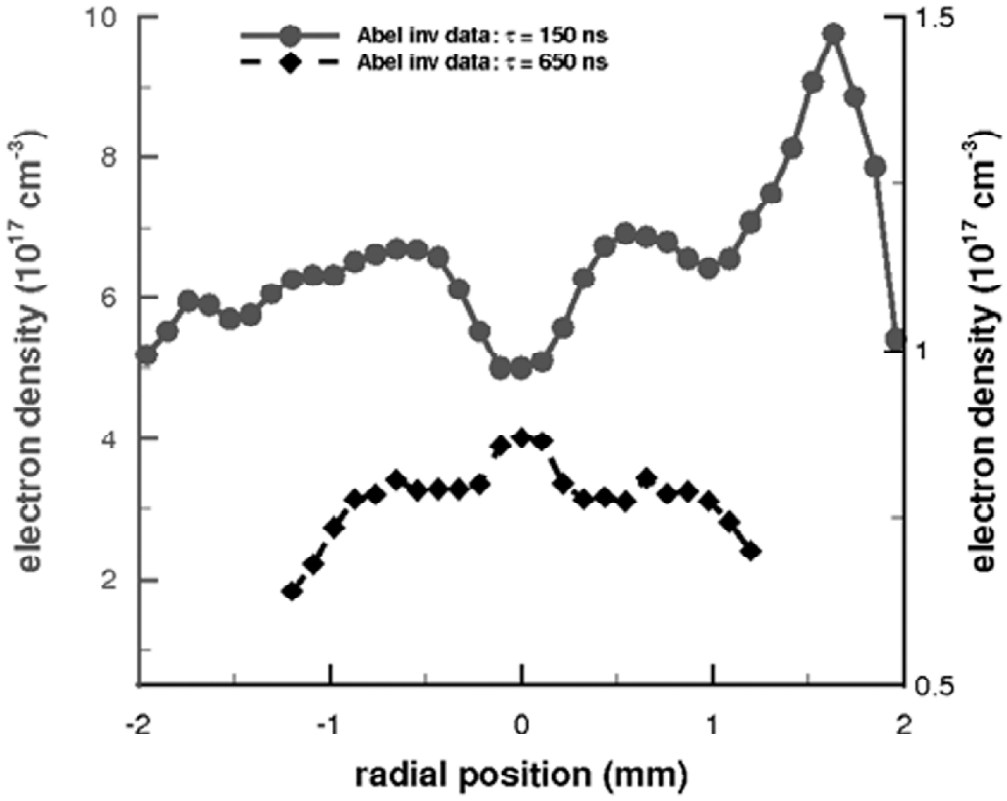

Figure 8: Electron densities *versus* radial position for 150 ns time delay (N_e axis on the left) and for 650 ns time delay ($N_e$axis on the right)

the electron density for values larger than 3 to 5 × 10^{17}cm^{-3} should be investigated using Abel inverse transforms of the Balmer series hydrogen alpha line to further elucidate the electron densities in the center of the laser-induced plasma. In turn, the 650 ns data indicate a peak near the center position, and the 650 ns Abel-inverted data lead to electron densities of the order of ~ 1 × 10^{17}cm^{-3} (N_e axis on the right). For the 650 ns time delay data, only data recorded in the lateral range of z = 1.1 mm to z = +3.3 mm were considered for Abel inversion due to smaller line-profile full-width-half-maxima than for the 400 ns time delay. Furthermore, a decrease in the signal-to-noise ratio occurred that would lead to larger error margins for the Abel inverse transforms of the recorded data for the 650 ns time delay from optical breakdown.

4. DISCUSSION AND CONCLUSIONS

The determination of the electron density distribution across the plasma can be accomplished by use of an Abel inversion with extension to slightly asymmetric plasma kernels. Filtering algorithms were not needed due to the choice of a series solution that has been extensively tested to work without pre-conditioning the wavelength and sensitivity corrected data. The results indicate close to spherical symmetry with a sphericall shell structure for the 150 ns and 400 ns time delay data sets and radial variations that are of the order of a factor of ~ 2 early in the plasma decay, with a diminishing difference for later time delays from optical breakdown. Similar results are expected to be found following inversion of time-resolved hydrogen alpha spectra; however, this is of continued interest. The insights gained from the application of the Abel inverse transform include the extraction of spatially resolved spectra along the line-of sight of the primarily spherical distribution of the expanding plasma kernel for time delays of 150 to 650 ns. The spatial variation of the electron density can be associated with the plasma expansion following laser-induced optical breakdown. The spatial variation of the hydrogen alpha and gamma lines together with the hydrogen beta results will be studied in future work to allow one to reconstruct the radial variation of the electron temperature using the so-called Boltzmann plot approach.

Acknowledgements

The authors acknowledge support in part by the Center for Laser Applications at The University of Tennessee Space Institute.

References

[1] A. W. Miziolek, V. Palleschi, I. Schechter (eds.), *Laser-Induced Breakdown Spectroscopy (LIBS) Fundamentals and Applications*, Cambridge University Press, New York (2006).

[2] R. E. Falcon, G. A. Rochau, J. E. Bailey, J. L. Ellis, A. L. Carlson, T. A. Gomez, M. H. Montgomery, D. E. Winget, E. Y. Chena, M. R. Gomez, T. J. Nash, Cornell University Library, Astro-Ph (2012) http://arxiv.org/abs/1210.7197v1 [accessed Nov 15, 2015].

[3] R. E. Falcon, G. A. Rochau, J. E. Bailey, T. A. Gomez, M. H. Montgomery, D. E. Winget, T. Nagayama, Astrophys. J. **806** (2015) 214.

[4] J. Radon, Ber. Sächs. Akad. Wissenschaft. Leipzig Math. Phys. Kl.**69** (1917) 262.

[5] J. Radon, IEEE Transact. Medical Imaging. **5** (1986) 170.

[6] H. J. Kunze, *Introduction to Plasma Spectroscopy*, Springer, Heidelberg (2009).

[7] A. M. Cormack, J. Appl. Phys. **34** (1963) 2722.

[8] A. M. Cormack, J. Appl. Phys. **35** (1964) 2908.

[9] S. R. Deans, *The Radon Transform And Some Of Its Applications*, John Wiley & Sons, New York (1983).

[10] S. Merk, A. Demidov, D. Shelby, I. B. Gornushkin, U. Panne, B. W. Smith, N. Omenetto, Appl. Spectrosc. **67** (2013) 851.

[11] M. Burger, M. Skočić, S. Bukvić, Spectrochim. Acta B. **101** (2014) 51.

[12] C. Killer, http://www.mathworks.com/matlabcentral/fileexchange/43639-abel-inversion-algorithm (2014) [accessed Nov 15 2015].

[13] G. Pretzler, Z. Naturforsch. **46a** (1991) 639.

[14] M. W. Blades, G. Horlick, Appl. Spectrosc. **34** (1980) 696.

[15] M. W. Blades, Appl. Spectrosc. **37** (1983) 371.

[16] S. Djurović, M. Ćirišan, A. V. Demura, G. V. Demchenko, D. Nikolić, M. A. Gigosos, and M. Á. Gonzáles, Phys. Rev. E. **79** (2009) 046402.

[17] J. M. Palomares, J. Torres, M. A. Gigosos, J. J. A. M. van der Mullen, A. Gamero, A. Sola, Appl. Spectrosc. **63** (2009) 1023.

[18] J. M. Palomares, J. Torres, M. A. Gigosos, J. J. A. M. van der Mullen, A. Gamero, A. Sola. J. Phys.: Conf. Ser. **207** (2010) 012013.

[19] H. Sobral, M. Villagrán-Muniz, R. Navarro-González, A. C. Raga, Appl. Phys. Lett. **77** (2000) 3158.

[20] M. Thiyagarajan, J. E. Scharer, IEEE Trans. Plasma Sci. **36** (2008) 2512.

[21] G. B. Arfken, H. J. Weber, F. E. Harris, *Mathematical Methods for Physicists, Seventh Edition: A Comprehensive Guide*, Academic Press, New York (2013).

[22] C. G. Parigger, D. H. Plemmons, E. Oks, Appl. Opt. **42** (2003)5992.

[23] G. Gautam, C. G. Parigger, D. M. Surmick, A. M. EL Sherbini, J. Quant. Spect. Radiat. Transf. **170** (2016) 189.

[24] C. G. Parigger, G. Gautam, A. C. Woods, D. M. Surmick, J. O. Hornkohl, Trends Appl. Spectrosc. **11** (2014) 1.

[25] C. G. Parigger, D. M. Surmick, G. Gautam, A. M. EL Sherbini, Opt. Lett. **40** (2015) 3436.

[26] D. M. Surmick, C. G. Parigger. Int. Rev. At. Mol. Phys. **5** (2014) 71.

[27] N. Konjević, M. Ivković, N. Sakan, Spectrochim. Acta B. **76** (2012) 16.

[28] M. Ivković, N. Konjević, Z. Pavlović, J. Quant. Spect. Radiat. Transf. **154** (2015) 1.